

## Full Length Article

# Microstructure formation and high temperature oxidation behavior of Ti-Al-Cr-Y-Si coatings on TiAl

Radosław Swadźba<sup>a,\*</sup>, Peter-Philipp Bauer<sup>b</sup>

<sup>a</sup> *Lukasiewicz Research Network - Institute for Ferrous Metallurgy, Gliwice, Poland*

<sup>b</sup> *DLR, German Aerospace Center, Institute of Materials Research, 51170 Cologne, Germany*



## ARTICLE INFO

## Keywords:

$\gamma$ -TiAl  
Coatings  
Deposition  
High temperature oxidation  
Reactive element effect

## ABSTRACT

The paper presents the application of Closed Hollow Cathode Physical Vapor Deposition (CHC-PVD) method for the deposition of Ti-Al-Cr-Y-Si coatings on  $\gamma$ -TiAl 48-2-2 alloy for high temperature oxidation protection. The study concerned the analysis of the coating's growth mechanism, initial microstructure as well as phase transformations investigations using high resolution Scanning Transmission Electron Microscopy (STEM) and high temperature X-ray diffraction (HT-XRD). The coated alloy was subjected to high temperature oxidation test at 850 °C where a fivefold lower mass gain compared to bare 48-2-2 alloy was observed. Detailed microstructural investigations allowed to characterize the thermally grown oxide scale, which was found to be composed of nanometric layers of titania, equiaxed  $(Al,Cr)_2O_3$  and columnar alumina. These investigations provided microstructural evidence for the Cr effect on the formation of  $Al_2O_3$ , which was postulated previously. Yttrium was found to segregate to the grain boundaries of alumina oxide scale during high temperature oxidation, indicating the occurrence of the reactive element effect.

## 1. Introduction

Intermetallics based on the  $\gamma$ -TiAl phase have been of great interest for major aircraft engine manufacturers, such as General Electric, Pratt & Whitney with MTU and Rolls-Royce, and are considered as a lighter alternative for Ni-base superalloys [1,2]. However, the application of TiAl-based alloys in air is limited to around 750–800 °C. This is related to the quick formation of mixed  $TiO_2 + Al_2O_3$  oxide scales upon exposure to air atmosphere and formation of nitrides, e.g.  $TiN/Ti_2AlN$  [3–6], at the metal-scale interface, that inhibit the formation of a continuous alumina layer [4,7].

It has been found that the addition of Cr to TiAl alloys may lead to formation of the ternary  $Ti(Cr,Al)_2$  Laves phase which is capable of protective alumina scale formation at 1000 °C in dry oxygen, despite an Al content of only 37–42 at.% [8,9]. Interestingly, binary Ti-Al alloys require as much as 49 at.% Al to form a protective alumina scale at 1000 °C in dry oxygen [7]. Brady et al. [8,9] proposed two mechanisms behind the Cr effect: reduced oxygen permeability by formation of the  $Ti(Cr,Al)_2$  Laves phase and negation of the adverse effects on oxidation of the nitrogen present in air. It has been postulated by Fox-Rabinovich et al. [10] that the 'Cr' effect is associated with the initial nucleation

and growth of the Cr doped alumina. Luthra [11] stated that chromium lowers the activity of titanium compared to that of Al and allows for alumina formation at lower Al levels.

Due to their exceptional high temperature oxidation resistance, the Ti-Al-Cr alloys have been proposed and successfully utilized as protective coatings deposited using Physical Vapor Deposition (PVD) method on a variety of TiAl intermetallics [12–17]. Moreover, it has been shown that the addition of small amounts (e.g. 0.1–0.3 at.%) of Reactive Elements, such as yttrium, is effective in enhancing the oxidation resistance of TiAl alloys leading to suppression of the outermost titania scale formation [18,19]. Higher Y levels resulted in higher oxidation rates under both isothermal and cyclic oxidation conditions [19]. It has also been found that the addition of Hf and Y as well as Si improves the adherence of the oxide scale [20]. Laska et al. [12] showed that modification of Ti-Al-Cr coatings with either Y or Zr (1 at. % and 4 at. %, respectively) further improves their high temperature oxidation resistance on TNB alloy at 850 °C. Similar coatings have also been successful for 48–2-2 and TNM-B1 alloys at 850 and 950 °C [13]. It has been suggested that yttrium segregates to the grain boundaries of  $\alpha$ - $Al_2O_3$  oxide scales [21], most likely providing a similar effect as it is the case for Ni-base superalloys [22]. Furthermore, the Ti-Al-Cr coatings modified with RE

\* Corresponding author.

E-mail address: [rswadzba@gmail.com](mailto:rswadzba@gmail.com) (R. Swadźba).

<https://doi.org/10.1016/j.apsusc.2021.150191>

Received 7 March 2021; Received in revised form 12 May 2021; Accepted 19 May 2021

Available online 24 May 2021

0169-4332/© 2021 The Authors.

Published by Elsevier B.V. This is an open access article under the CC BY-NC-ND license

(<http://creativecommons.org/licenses/by-nc-nd/4.0/>).

were successfully applied as bondcoatings for Thermal Barrier Coatings (TBCs) providing high lifetimes at temperature in the range of 900–1000 °C [12,15,21].

The goal of this paper was to explore the possibility to deposit Ti-Al-Cr-Y-Si coatings using Closed Hollow Cathode PVD (CHC-PVD) method on 48-2-2 TiAl alloy. The scope of this work included investigations aimed at understanding the coatings growth mechanism and subsequent evolution during high temperature oxidation at 850 °C. High resolution scanning electron microscopy (STEM) was utilized to study the substructure of the coating with regard to the segregation of dopants, i.e. Si and Y, both within it as well as in the thermally grown oxide scales.

## 2. Experimental procedure

The base material was the 48-2-2 TiAl alloy provided by GfE GmbH from Germany, containing 48% Al, 2% Cr, 2% Nb (all in atomic %) and balance Ti. The alloy was cast to an ingot with 80 mm of diameter from which bars with diameter of 15 mm were cut using Electro Discharge Machining (EDM) method. The bars were then cut to coupons with thickness of 2 mm and EDM was used to drill holes with diameter of around 1.8 mm for hanging purposes. The samples were ground with 800 grit SiC paper and cleaned in ultrasonic cleaner. Afterwards, one of the samples was coated with Ti-Al-Cr-Si-Y coating using a Closed Hollow Cathode Physical Vapor Deposition (CHC-PVD) method on a prototype system developed in cooperation with Fraunhofer IST, Braunschweig, Germany. The CHC-PVD method has been successfully utilized to modify aluminide coatings with Pt [23,24] and due to its high density plasma it allows to produce uniform coatings with high deposition rates. In the process, the sample was hung within the hollow cathode with diameter of 80 mm and length of 160 mm and nominal composition Ti-54Al-14Cr-0.5Si-0.5Y (all in at. %), produced by Matsurf Technologies Inc., USA. Prior to coating deposition the sample was subjected to argon ion bombardment using 150 V bias voltage in order to remove contamination from its surface. The coating deposition power was 500 W and the argon pressure was maintained at 0.5 mbar Ar for 4 h. The samples were subjected to high temperature oxidation test at 850 °C for 288 h in laboratory air. After 24, 96, 168 and 288 h the samples were removed from the furnace, cooled in static air and weighted using an analytical balance with accuracy of  $10^{-5}$  g. After the oxidation test the microstructure of the samples was investigated using a Field Emission Gun (FEG) equipped Scanning Electron Microscope (SEM) JEOL JSM 7200F, operating at 15 kV accelerating voltage and equipped with EDS and EBSD detectors by EDAX. The phase identification using EBSD method was aided with the ICDD-PDF-4 database. The high resolution investigations of the coating as well as the thermally grown oxide scale formed during high temperature oxidation experiments were performed using a Cs-corrected Scanning Transmission Electron Microscope (STEM) FEI TITAN 80-300 operating at 300 kV with Z-sensitive High Angle Annular Dark Field (HAADF) and Annular Dark Field (ADF)

detectors. The chemical composition of the oxidation products was studied using Energy Dispersive Spectroscopy (EDS) under STEM mode. The samples for STEM investigations were prepared using Focused Ion Beam (FIB) on a FEI Quanta 3D 200i dual-beam system. During the FIB preparation of samples Pt layers ( $15 \mu\text{m} \times 2 \mu\text{m} \times 2 \mu\text{m}$ ) were applied on top of the samples to protect them during the gallium ion thinning process. The phase composition at elevated temperatures, up to 900 °C, was studied using Bruker D8 Advance system equipped with a high temperature chamber HTK 1200 N by Anton Paar utilizing a copper tube.

## 3. Results

### 3.1. Microstructure characterization of the as-deposited coating

The surface microstructure of the as-deposited Ti-Al-Cr-Y-Si coating is presented in in Fig. 1a and b. As shown in the atomic number sensitive (i.e. Z-contrast) SEM-BSE image (Fig. 1a), the coating's surface consists of cauliflower-like microstructure that also inherited the roughness of the underlying substrate. It is visible as grooves originating most likely from the surface preparation prior to coating deposition. Moreover, as shown in SEM-SE image (Fig. 1b), the coating consists of nanometric and densely packed grains. The chemical composition measured in the area marked in Fig. 1b is presented in Table 1 and is close to the composition of the applied compound target used in the CHC-PVD process.

The cross-sectional microstructure of the as-deposited coating is presented in SEM-BSE image in Fig. 2. It was found that the interface between the coating and the substrate is clean and continuous with a clear boundary between them. As shown in Fig. 2 the coating grew in the form of columns widening towards the surface to the width of around 3  $\mu\text{m}$ , while the total coating thickness was found to be around 13  $\mu\text{m}$ . In the EDS elemental mapping of Ti, Cr, Al and Nb, shown in Fig. 2, it is visible that the distribution of all the elements in the coating is uniform and that the inward diffusion of elements to the substrate did not occur. The chemical composition of the coating in the cross-section is similar to that found on the surface – around 57 at. % of Al, 15 at. % Cr and low amounts of Si and Y with balance of Ti.

In order to characterize the microstructure of the Ti-Al-Cr-Si-Y coating in the as-deposited condition detailed STEM and TEM investigations were performed and their results are shown in Fig. 3a-f. In the STEM-HAADF image (Fig. 3a) the feather-like substructure of the columns is visible. Similarly to the BSE images under SEM (Fig. 2), the

**Table 1**

Chemical composition of the TiAlCrYSi coating shown in Fig. 1b.

Element	Al	Si	Y	Ti	Cr
wt. %	37,6	0,8	0,8	37,4	23,4
at. %	52,3	1,0	0,4	29,4	17,0

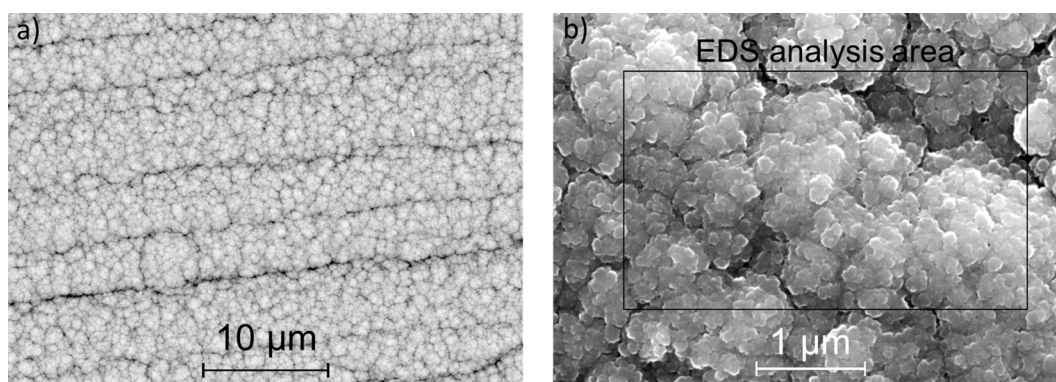


**Fig. 1.** Surface morphology of the as-deposited TiAlCrYSi coating: a) BSE and b) SE contrast.

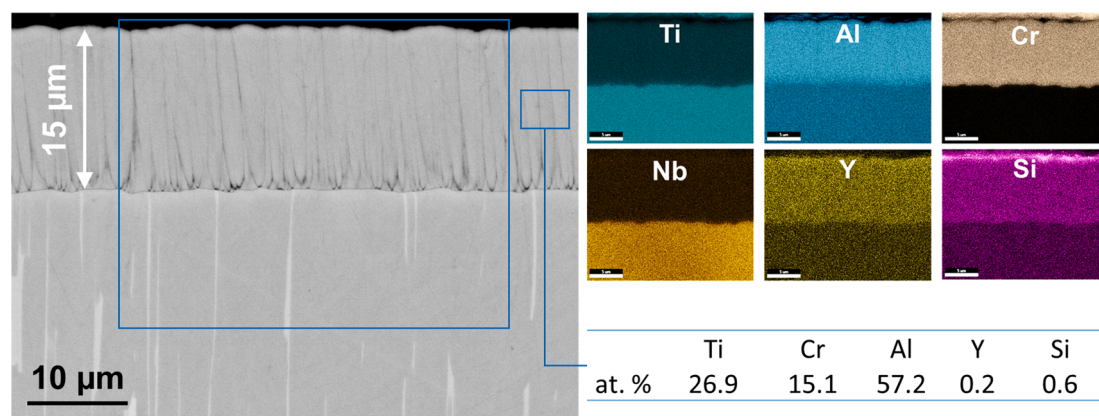


Fig. 2. Cross-sectional microstructure and the chemical composition of the as-deposited TiAlCrYSi coating along with elemental distribution of Ti, Al, Cr, Nb, Y and Si.

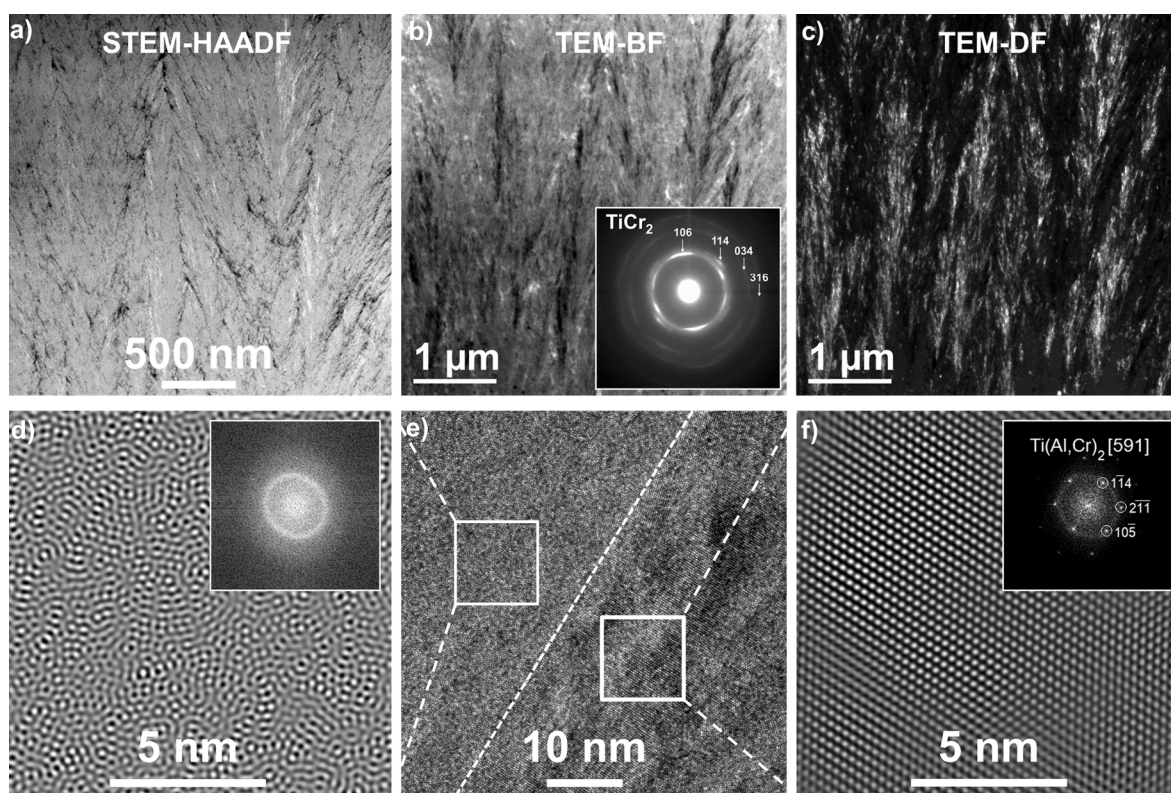


Fig. 3. Cross-sectional STEM-HAADF (a), b) TEM-BF and c) TEM-DF images of the as-deposited TiAlCrYSi coating. Fast Fourier Transform (FFT) and Inverse FFT images of the amorphous (d) and crystalline (f) areas marked in HRTEM image (e).

STEM-HAADF detector is sensitive to Z-contrast and therefore the image shown in Fig. 3a also reveals the uniformity of the chemical composition between the column feathers. The bright-colored areas in the STEM-HAADF image correspond to crystalline components of the microstructure with strong crystallographic misorientation compared to the surrounding area. This effect is obtained by the adjustment of the camera length under STEM mode, where the HAADF detector is capable of revealing the variations of both chemical composition and crystallographic orientation. Additionally, the feather-like microstructure along with variations in the orientation of particular grains is shown in TEM-BF (Fig. 3b) and TEM-DF images. Additionally, the insert in Fig. 3b shows electron diffraction obtained applying the Selected Area aperture from the cross-section of the coating. This Selected Area Diffraction pattern (SADP) was found to contain concentric rings indicating the

presence of numerous crystalline nanometric-sized grains with a strong texture in the growth direction of the coating. These grains are also visible in the TEM-DF image shown in Fig. 3c. Based on the measured distances of each ring from the center of the SADP, the presence of the TiAl phase was found and corresponding Miller indices were denoted. It was found that the (106) (or (10-16)) planes are arranged perpendicular to the growth direction of the coating. Furthermore, the High Resolution TEM (HRTEM) investigations performed within one of the columns indicated the presence of both amorphous as well as crystalline regions (Fig. 3d-f). As shown in Fig. 3e these areas are present adjacent to each other. The left-hand side of the image shown in Fig. 3e was found to be amorphous, as evidenced by the Inverse Fast Fourier Transform (IFFT – Fig. 3d) and Fast Fourier Transform (insert in Fig. 3d). The area on the right-hand side was found to be crystalline, which is presented in

the FFT and IFFT images shown in Fig. 3f. Moreover, based on the FFT image (insert in Fig. 3f) this area was identified as the  $\text{Ti}(\text{Al,Cr})_2$  phase.

### 3.2. Phase transformations during high temperature exposure at 850 °C

Since the as-deposited  $\text{TiAlCrYSi}$  coating was found to be partially amorphous with strongly textured crystalline regions, high temperature XRD investigations were performed in order to study potential phase transformations during initial high temperature exposure. The results of the HT-XRD are shown in Fig. 4 and contain the phase composition changes during the heat-up stage (lower part of the graph) as well as the phase transformations during annealing at 850 °C for 24 h in air (upper part of the graph). The peak broadening in the as-deposited condition may result from the presence of the amorphous regions in the coating, while the drifting of the peak to lower  $2\theta$  values upon heating most likely originates from variations of  $d$  lattice plane distances. During heating, the only detected peak is (106) from the hexagonal  $\text{Ti}(\text{Al,Cr})_2$  phase (PDF 47-1716,  $P63/mmc$  (194)), which is indicative of strong texture and in good agreement with the TEM results, shown in Fig. 3. At around 700 °C new peaks begin to appear, that correspond to the Laves  $\text{AlCr}_2$  phase (PDF 29-0016,  $P4/mmm$  (123)), which most likely crystallized in the amorphous regions, and remain present throughout the whole experiment. During heating, the intensity of the  $\text{Ti}(\text{Al,Cr})_2$  (106) peak increases and sharpens, which may indicate onset of the amorphous component's crystallization. Additionally, after around 4 h of exposure at 850 °C new peaks ((111) and (200)) from the tetragonal  $\gamma$ - $\text{TiAl}$  phase appear (PDF 05-0678,  $P4/mmm$  (123)), while the initially very strong (106) peak of the  $\text{Ti}(\text{Al,Cr})_2$  starts to fade. The measurements performed after reaching 850 °C also revealed the formation of the  $\alpha_2$ - $\text{Ti}_3\text{Al}$  phase (PDF 00-052-0859,  $P63/mmc$  (194)). It is suggested that the strongly textured Laves phase, which formed during the coating deposition, decomposes and new  $\gamma$ - $\text{TiAl}$  and  $\alpha_2$ - $\text{Ti}_3\text{Al}$  grains are formed, devoid of texture. Additionally, new  $\alpha$ - $\text{Al}_2\text{O}_3$  peaks start to form which is related to the growth of the oxide scale, that certainly started earlier but due to its low thickness it was not possible to capture it using XRD.

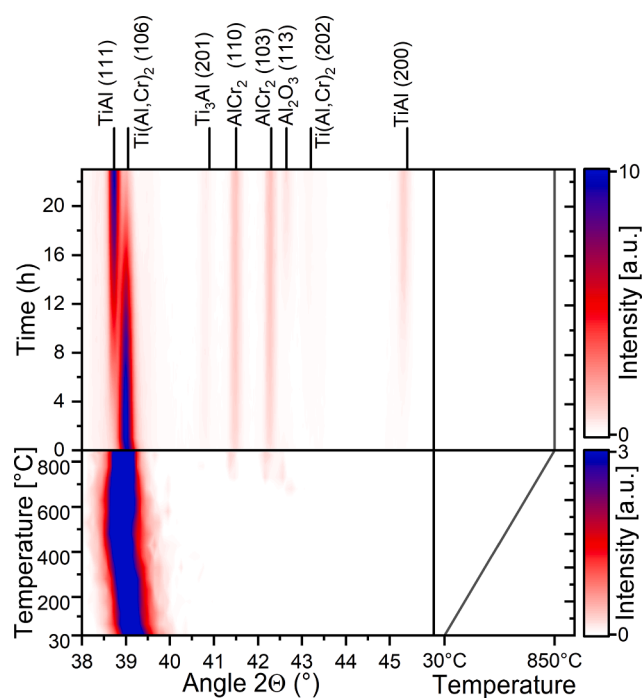


Fig. 4. High Temperature XRD (HT-XRD) results showing phase transformations in the Ti-Al-Cr-Y-Si coating during heat-up and holding at 850 °C for 24 h hours in air.

### 3.3. High temperature oxidation behavior at 850 °C

The oxidation behavior of the obtained Ti-Al-Cr-Y-Si coating was evaluated in high temperature oxidation test performed at 850 °C and compared to bare TiAl alloy. Mass change diagrams vs oxidation time were plotted in the column chart, shown in Fig. 5a, along with images presenting the visual appearance of the samples after the test (Fig. 5b,c). As presented in Fig. 5, already after the first 24 h of oxidation the bare alloy exhibited a rapid mass gain of around 0.90  $\text{mg}/\text{cm}^2$ . It is 6x higher compared to the sample coated with Ti-Al-Cr-Si-Y coating, that gained around 0.15  $\text{mg}/\text{cm}^2$ . This trend continued for the whole duration of the test and the ratio of the mass gain between the coated and uncoated TiAl samples remained around 5-6x. After the 288 h of oxidation at 850 °C the total mass gain of the bare TiAl reached 1.84  $\text{mg}/\text{cm}^2$ , while that of the Ti-Al-Cr-Si-Y coated sample was around 0.35  $\text{mg}/\text{cm}^2$ . The visual inspection of the samples after the test, shown in Fig. 5b and c, revealed that after the oxidation test the bare TiAl sample was characterized by different shades of yellow, indicating various scale thicknesses. Also, significant spallation of the oxide scale was observed in the vicinity of the edges of the sample as well as near the hole used for hanging. On the other hand, the Ti-Al-Cr-Si-Y coated sample after the oxidation test was covered by a continuous oxide scale with a green shade. Moreover, no spallation of the oxide scale was observed either on flat surface or sharp edges of the sample. Besides the mass measurements during the oxidation tests, the surface microstructures of the samples were studied using SEM after 24, 96, 168 and 288 h. The results shown in Fig. 6 for bare TiAl indicate the formation of a mixed oxide scale, composed of a continuous passivating layer and faceted bright grains. Based on the chemical composition analysis, shown in Table 2, it is suggested that the former part of the oxide scale is most likely alumina (area 1 in Fig. 6 and Table 2), while the latter is most likely titania (area 2 in Fig. 6 and Table 2). Previous research works also indicated that titania formation may be visible as yellow colored [25,26]. Moreover, the progress of oxidation in the sample area studied on bare TiAl after various oxidation times shows the continuous formation of new titania grains and their expansion. On the other hand, the surface microstructure of the Ti-Al-Cr-Si-Y coated sample remained somewhat unchanged during the whole oxidation test. The chemical composition of the oxide scale formed on the coating (area 3 in Fig. 6 and Table 2) indicates that it is composed in majority of alumina with some titania. As shown in Fig. 6, the grooves that were present in the as-deposited condition remained visible between 24 and 288 h, indicating the formation of a very thin oxide scale.

The microstructure of the Ti-Al-Cr-Si-Y coating after the 288 h of oxidation at 850 °C is presented in Fig. 7. As shown in the SEM-BSE image in Fig. 7a the coating is around 25  $\mu\text{m}$  thick and consists of two distinctive zones. The outer zone contains a mixture of bright areas that constitute the base of the coating, with elongated gray grains dispersed in them. Moreover, numerous voids were found to be distributed uniformly all over the coating. The inner zone, present at the interface between the coating and the substrate, contains alternately situated gray and bright grains, elongated perpendicular to the surface. On top of the coating an oxide scale with the thickness of approximately 250 nm was found. Interestingly, underneath the oxide scale numerous oxide pockets could also be observed, reaching around 2  $\mu\text{m}$  into the coating. Based on the elemental mapping shown in Fig. 7b-g it is visible that the coating is enriched in Cr (Fig. 7c), which is segregated to the bright grains, both in the inner and outer zone of the coating. Based on the distribution of Ti (Fig. 7b) it is visible that its content is lower in the coating than in the substrate alloy and slightly higher in the gray grains than bright ones. The Al (Fig. 7d) distribution reveals that it is segregated mostly to the elongated gray grains as well as the oxide scale, where oxygen is also visible (Fig. 7e). Additionally, some oxygen rich regions could also be observed at the interface between the coating and the substrate. The distribution of the trace elements present in the coating, i.e. Y and Si (Fig. 7f and g) indicates that the former is distributed uniformly within the coating while Si is segregated more to the elongated gray grains. In

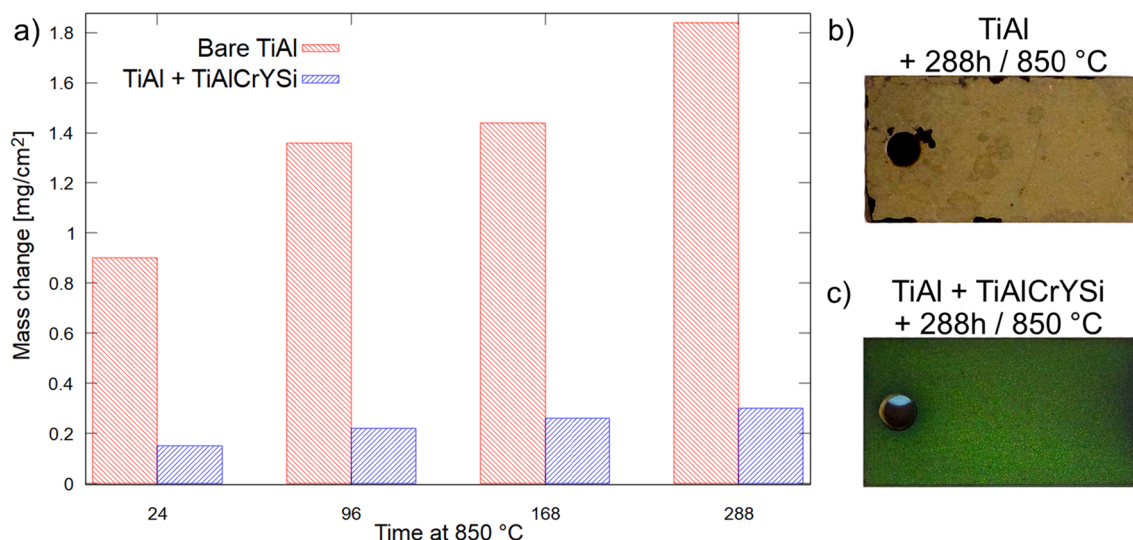


Fig. 5. Mass change diagram versus oxidation time at 850 °C (a) of b) bare and c) TiAlCrYSi coated TiAl.

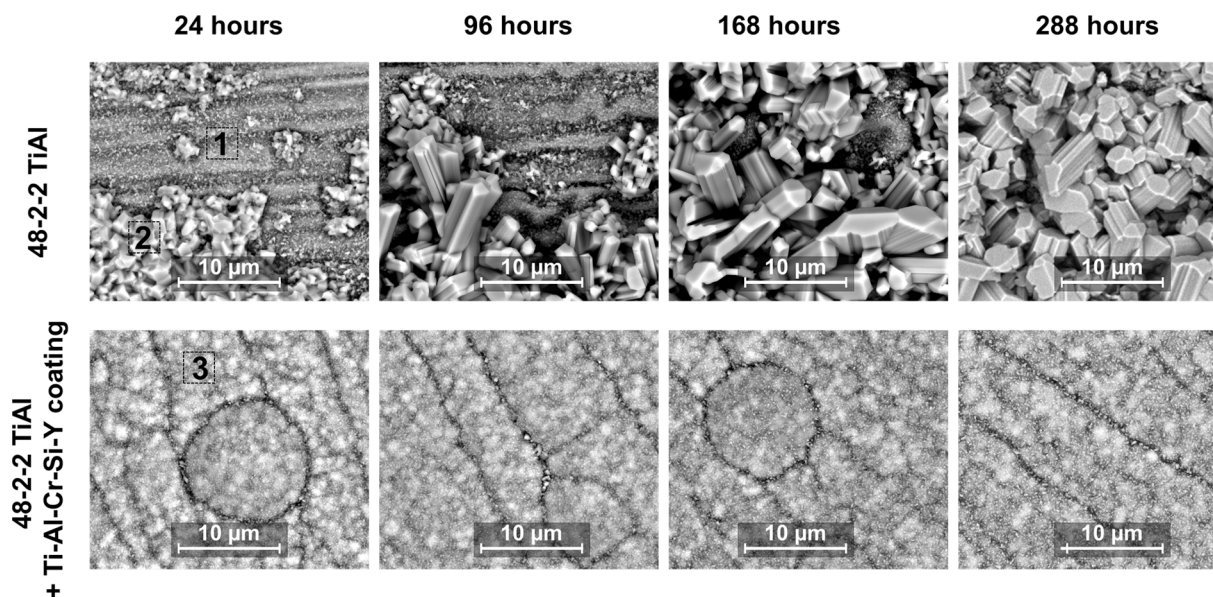


Fig. 6. Surface morphology evolution of bare and TiAlCrYSi coated TiAl during oxidation at 850 °C.

Table 2  
Chemical composition (at. %) of the micro-areas 1–3 marked in Fig. 6.

	1	2	3
O	48,3	55,3	44,3
Al	27,9	2,6	37,4
Nb	0,9		
Ti	22,0	42,2	12,5
Cr	0,9		5,8

order to identify the phase composition of the coating after the high temperature oxidation test, EBSD investigations were performed in the outer (Fig. 8a) and inner (Fig. 8b) zones of the coating. Additionally, the areas marked as 1–5 in Fig. 8a and b were studied using EDS and their chemical composition is presented in Table 3. Based on the EBSD results it was found that the oxide pockets (marked as 1 in Fig. 8a) are  $\alpha$ - $\text{Al}_2\text{O}_3$ , containing trace amounts of Ti, Si and Y (Table 3). The region marked as 2 in Fig. 8a corresponds to the gray grains visible in Fig. 7a. It was found that it contains around 60 at. % Al, 35 at. % Ti, 5 at. % Cr and minor

amounts of Si and Y. As indicated in the EBSD phase mapping (Fig. 8a) these grains were identified as tetragonal  $\gamma$ -TiAl. The region marked as 3 in Fig. 8a corresponds to the large bright areas visible in Fig. 7a. Moreover, the Image Quality (IQ) obtained using EBSD (Fig. 8a) revealed that in fact they are composed of numerous nanometric grains. They were identified as the Laves  $\text{TiCr}_2$  phase containing around 47 at. % Al, 29 at. % Ti and 22% at. Cr with trace amounts of Si and Y. Moreover, the grains situated at the interface between the coating and substrate, marked as 4 in Fig. 8b, were found by  $\gamma$ -TiAl, similarly to grains marked as 2 in Fig. 8a. However, their chemical composition varied slightly (points 2 and 4 in Table 3) as they contained more Al (61 at. %), and Cr (6 at. %) as well as less Ti (32 at. %) and no Si or Y. Also, 0.7 at. % of Nb was found to be present in these grains, which was not found in grains marked as 2 in Fig. 8a. The elongated grains that are marked as 5 in Fig. 8 correspond to the bright grains visible in Fig. 7a. Similarly to grains marked as 3 in Fig. 8a they were also identified as Laves  $\text{TiCr}_2$  phase with higher Al, Cr and Ti contents, 42 at. %, 30 at. % and 26 at. %, respectively (Table 3).

As shown in Fig. 7f and g the elements introduced to the coating in

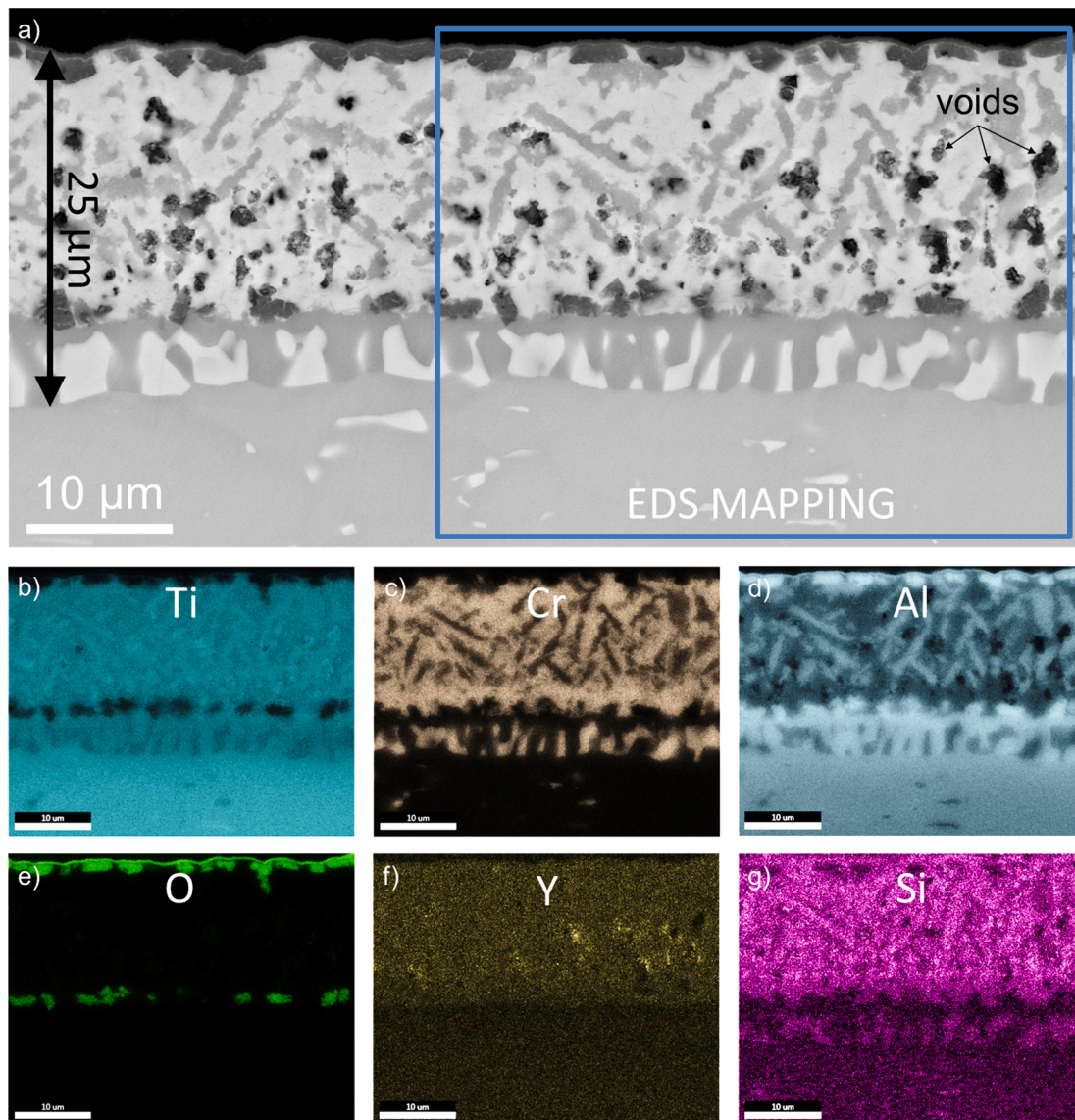
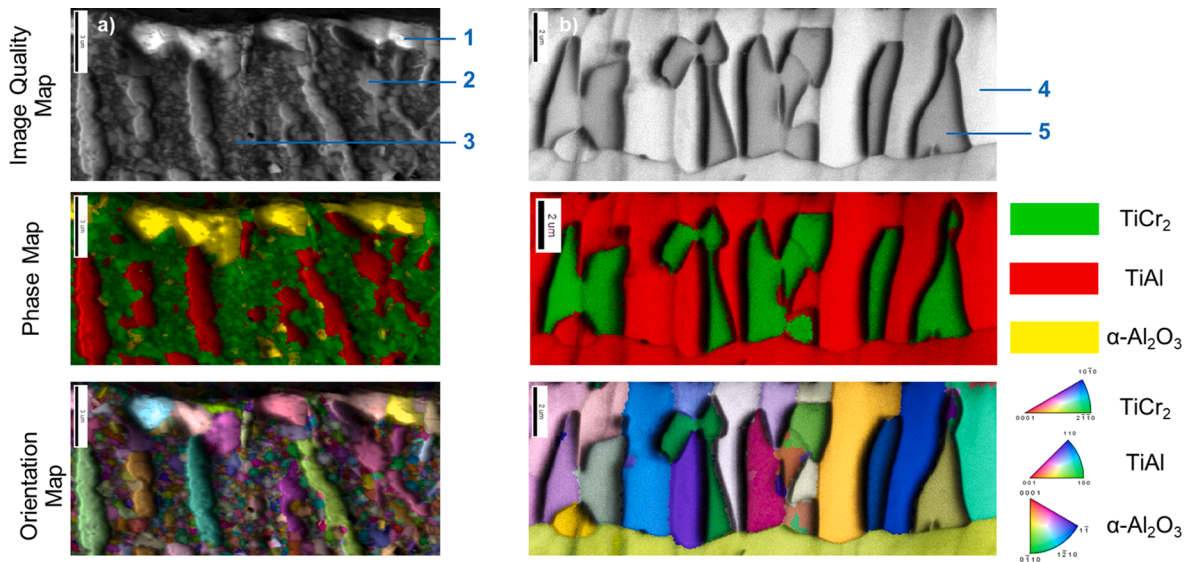


Fig. 7. Cross-sectional microstructure of the TiAlCrYSi coating after 288 oxidation at 850 °C (a) and elemental mapping of b) Ti, c) Cr, d) Al, e) O, f) Y and g) Si.

very low quantities, i.e. Si and Y, were found to be somewhat uniformly distributed in the cross-section of the coating. In order to investigate its microstructure in more detail, STEM investigations were performed and their results are shown in Figs. 9 and 10. The SEM-BSE image of the Ti-Al-Cr-Si-Y coating (Fig. 9a) shows the bright  $\text{TiCr}_2$  and gray TiAl grains, while the STEM-HAADF image (Fig. 9b) reveals additional white precipitates, with diameter of around 250 nm. As indicated by the elemental distribution, shown in Fig. 9c-f, compared to their surroundings, these precipitates are enriched in Cr, and depleted in Al and Ti. Electron diffraction phase identification showed that these precipitates are  $\text{AlCr}_2$  phase. Additionally, as shown in Fig. 9b, the TiAl phase grains contain a variety of nanometric-sized precipitates distributed uniformly within them. Moreover, Si distribution (Fig. 9f) indicates that it is present in the  $\text{Ti}(\text{Al},\text{Cr})_2$  grains. Additionally, very fine and elongated Ti-rich precipitates, as well as round nanometric-sized Nb- and Y-rich precipitates could also be found (Fig. 9e, g and h). A more detailed STEM-ADF image, shown in Fig. 10a, illustrates the morphology and distribution of the identified Si-rich  $\text{TiCr}_2$  and  $\text{Ti}_3\text{Al}$  grains. Moreover, HRTEM investigations revealed the presence of very fine precipitates with diameter of around 10–15 nm, shown in Fig. 10b. Based on the IFFT (Fig. 10c) and FFT (Fig. 10d) images these precipitates were identified to be  $\text{Y}_2\text{O}_3$ . The electron diffraction patterns for the  $\text{Ti}_3\text{Al}$  and Si-rich  $\text{TiCr}_2$

are shown in Fig. 10e and f.

To understand the oxidation behavior of the Ti-Al-Cr-Si-Y coating during 288 h at 850 °C, STEM investigations of the oxide scale were performed (Figs. 11 and 12). The cross-sectional microstructures shown in Fig. 11a and b show the outer oxide layer using STEM-ADF and STEM-HAADF detectors, respectively. While the latter was described in the previous section, the STEM-ADF detector allows for visualization of grains varying in crystallographic orientation. The combination of both these detectors as well as EDS elemental mapping, shown in Fig. 11c-f, makes it possible to characterize in detail the formed oxide scale. It is visible that the outer oxide scale consists of three zones and its total thickness is around 220 nm. The outer zone is around 60 nm and consists of Ti and O, as shown in Fig. 11d and f. The middle zone consists of equiaxed grains containing Al, Cr and O (Fig. 11c, e and f, respectively) while the inner zone is composed of thin columnar grains containing O and Al. Underneath this very thin outer oxide scale the  $\alpha\text{-Al}_2\text{O}_3$  pockets were found, as described in previous paragraphs. The EBSD phase and orientation maps, shown in Fig. 8a, reveal the presence of multiple  $\alpha\text{-Al}_2\text{O}_3$  grains with high-angle grain boundaries within each pocket. Additional STEM investigations of the grain boundaries of these  $\alpha\text{-Al}_2\text{O}_3$  grains revealed that they appear bright in the Z-sensitive STEM-HAADF imaging, as shown in Fig. 12a, which is indicative of the presence of



**Fig. 8.** Cross-sectional image quality (IQ) results obtained using EBSD of the oxide scale-coating (a) and coating-alloy interfaces (b) along with phase and crystallographic orientation maps. The chemical composition from areas marked as 1–5 is shown in Table 3.

**Table 3**  
Chemical composition (at. %) of the micro-areas 1–5 marked in Fig. 8a and b.

	1	2	3	4	5
O	53,2				
Al	36,8	59,8	47,3	61,3	42,2
Si	0,2	0,3	1,2		0,4
Y	0,1	0,3	0,2		
Ti	6,3	34,8	29,4	32,0	30,1
Cr	3,3	4,8	21,8	6,0	26,1
Nb				0,7	1,3

elements with a higher atomic number than Al and O. The EDS elemental mapping performed in the window marked in Fig. 12a revealed the segregation of Y to the grain boundary of the studied  $\alpha$ -Al<sub>2</sub>O<sub>3</sub> grains (marked with arrows in Fig. 12b). Moreover, in the

vicinity of the grain boundary several Y-rich precipitates were also observed. Based on the HRTEM image, shown in Fig. 12c, one of them was identified as Y<sub>2</sub>O<sub>3</sub>.

**4. Discussion**

**4.1. Coating growth and initial microstructure formation**

Most of the recent publications on the Ti-Al-Cr-based coatings concerned their deposition using magnetron sputtering method using separate targets for each one of the elements [12,13,21]. A contrary approach was taken in this work, where the coating was deposited using the CHC-PVD method using a compound target containing all the elements that were planned to be present in the designed coating. It has been found that in the as-deposited condition the coating contains all the

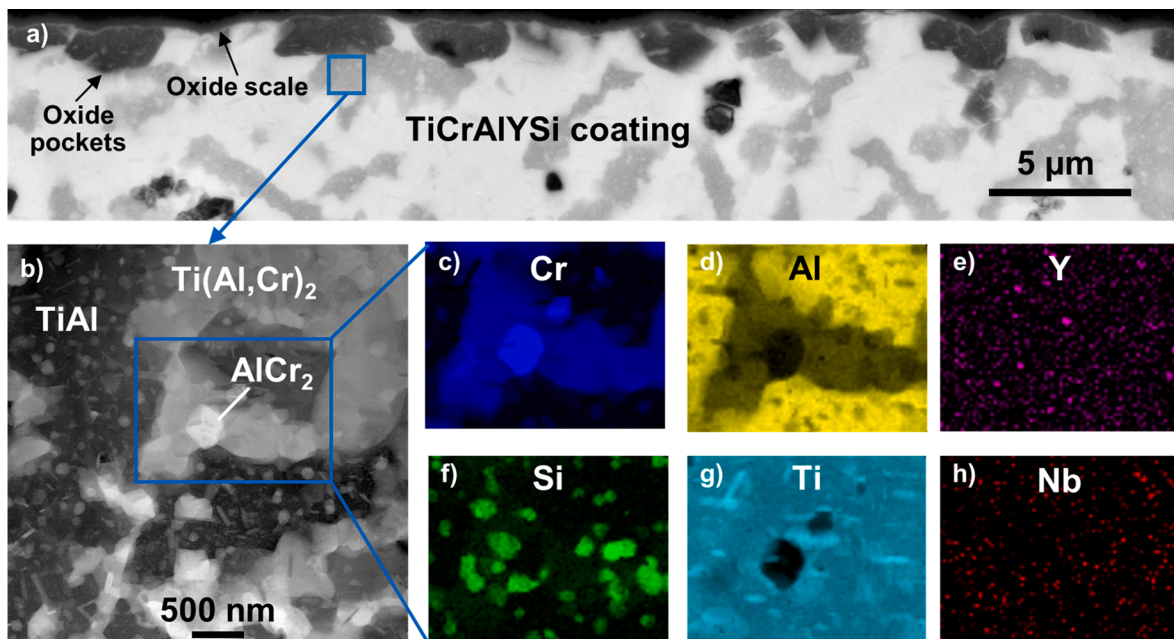


**Fig. 9.** SEM-BSE image of the TiAlCrYSi coating – oxide scale interface (a) along STEM-HAADF image (b) along with elemental distribution mapping of c) Cr, d) Al, e) Y, f) Si, g) Ti and h) Nb.

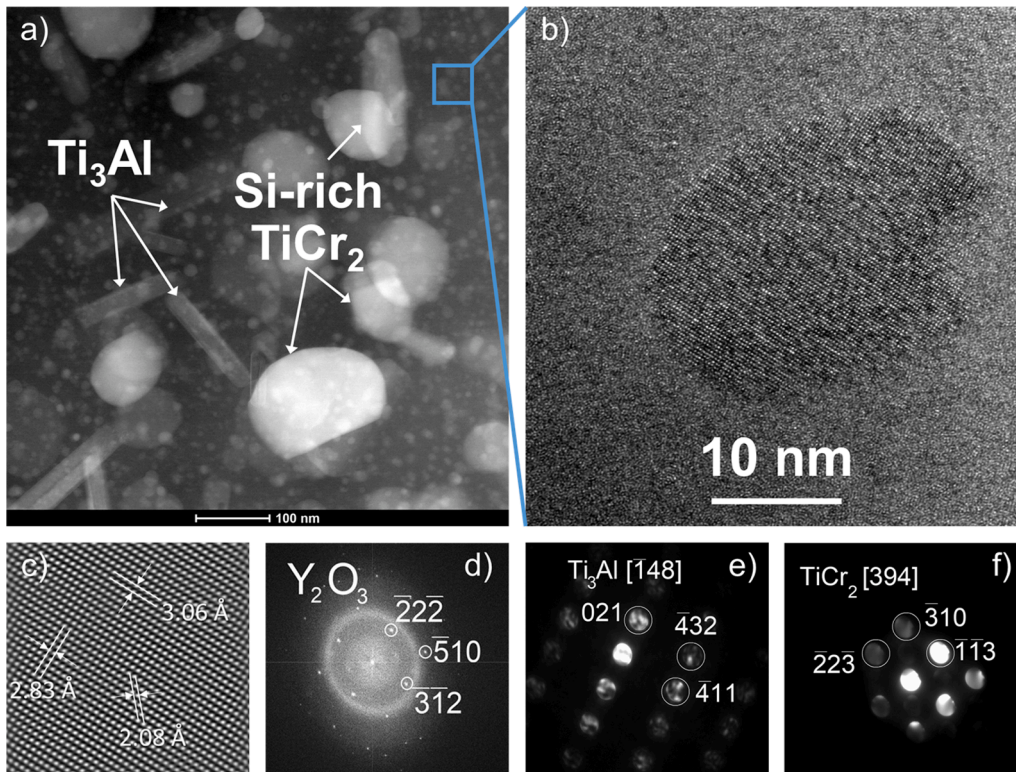


**Fig. 10.** STEM-ADF (a) and HRTEM (b) images of the TiAlCrYSi coating with visible nanometric  $Y_2O_3$  precipitate identified based on the IFFT (c) and FFT (d) images, as well as electron diffraction patterns for  $Ti_3Al$  (e) and  $TiCr_2$  (f).

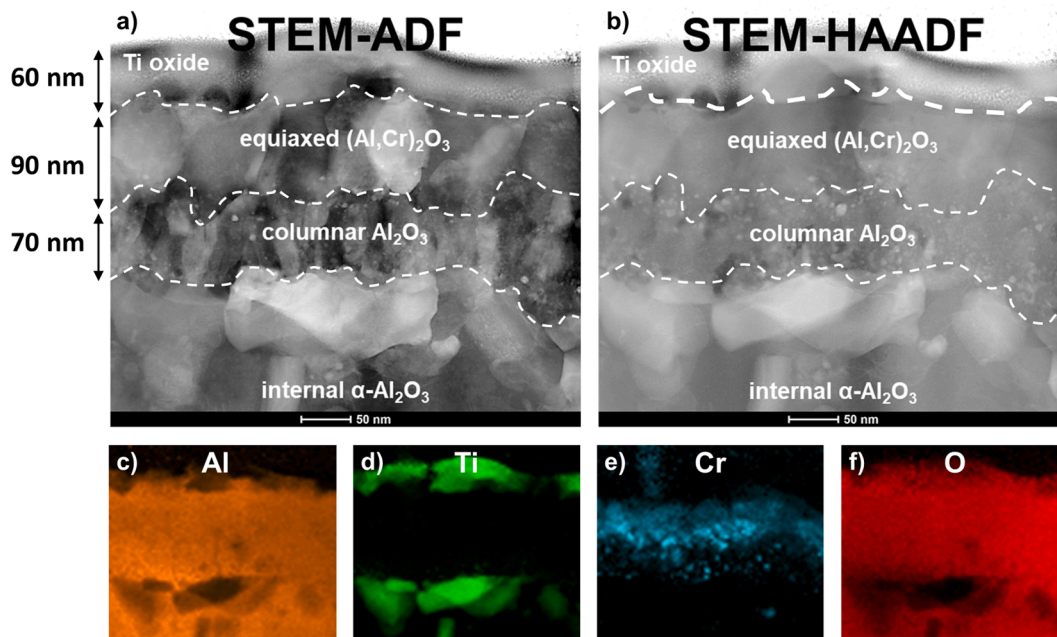


**Fig. 11.** Cross-sectional STEM-ADF (a) and HAADF (b) images of the outer oxide scale formed on the TiAlCrYSi coating during 288 h of oxidation at 850 °C along with elemental distribution of c) Al, d) Ti, e) Cr and f) O.

elements from the target uniformly distributed in its cross-section, without any visible segregation. The chemical composition of the coating was found to be in a reasonable agreement compared to the target's composition. The following differences were observed between the coating and the target: lower Ti (27% at. vs 31% at.), higher Al (57% at. vs 54% at.), similar Cr (15 at. % vs 14 at. %), similar Si (0.6 at. % vs 0.5 at. %) and lower Y (0.2 at. % vs 0.5 at. %). The minor differences

most likely originate from different sputtering yields, which is typical for PVD methods. Moreover, our unpublished results [27] as well as research works by others [16] indicated that applying additional bias voltage to the samples results in a higher Cr content in the coating at the expense of Al, especially in the corners of the samples, where the current density is highest. This effect was found to be detrimental for high temperature oxidation resistance [27].

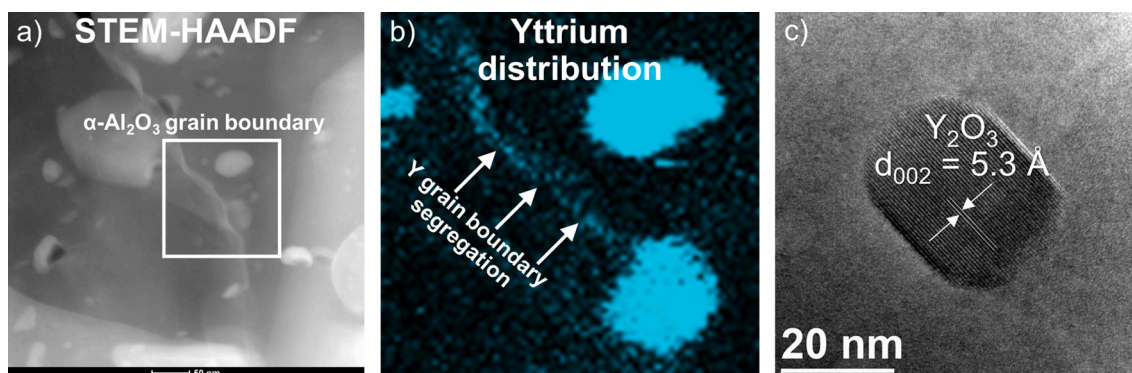


Fig. 12. STEM-HAADF image of the internal  $\alpha\text{-Al}_2\text{O}_3$  oxide scale showing a doped grain boundary (a), b) elemental mapping revealing segregation of Y and c) HRTEM image of  $\text{Y}_2\text{O}_3$  precipitate within the TGO.

Based on the Ti-Al-Cr diagram [28], the chemical composition of both the target and the obtained coating at  $800^\circ\text{C}$  lies in the field of C14 Laves (hexagonal  $\text{TiCr}_2$ ),  $\text{TiAl}_2$  and Cr phases. HT-XRD and TEM investigations of the as-deposited coating revealed only the presence of the strongly textured C14  $\text{TiCr}_2$  phase, while the remaining part of the coating was found to be amorphous. These results differ from the results of several research works on Ti-Al-Cr coatings [12,13,21,29], where the magnetron sputtered coatings were described as completely amorphous in the as-deposited state. However, the results of TEM investigations were not presented in these works. Other works have reported the formation of columnar and crystalline  $\text{TiAlCr}$  coatings, composed of gamma- $\text{TiAl}$  and Laves phases [30]. In fact, the coating studied in this work was characterized by a columnar microstructure with feather-like features, visible using STEM imaging, that are typical for the “Zone T” type of microstructure, as described by Thornton [31] as well as Movchan and Demchishin [32]. Such a microstructure forms when the temperature of the coating deposition process ( $T_s$ ) is in the range of 0.2–0.4 of the melting point of the deposited material ( $T_m$ ). In this  $T_s/T_m$  range the bulk diffusion is still negligible and the surface diffusion plays a major role in the coating growth mechanism [33,34]. During the initial stages of coating deposition nucleation and growth of randomly oriented islands occurs. These islands are characterized by a lateral size depending on the nucleation density. Upon further growth of the coating, surface diffusion leads to a competitive growth between various crystallographic orientations. The sites with low diffusivity, and thus low potential energy, become more favorable giving rise to the growth of textured V-shaped grains [33,34]. In the case of the studied coating, TEM investigations revealed that the (106) (or (10-16)) planes were arranged perpendicular to the direction of the coating’s growth, which was parallel to the [211] (or [10,11]) direction. This characteristic growth direction of the coating is most likely owed to the applied closed hollow cathode process, where the coated samples are stationary, while the geometry of the source is cylindrical. This somewhat mimics the effect of substrate rotation where the macroscopic shadowing of particular columns takes place and thus alters the vapor phase condensation.

#### 4.2. Microstructure and phase composition evolution at $850^\circ\text{C}$

The phase composition of the coating after the cyclic oxidation test is in agreement with previous research works on similar coatings, that reported formation of either hexagonal (C14) [12] or cubic (C15) [21] Ti (Al,Cr) $_2$  Laves phase, in addition to the Al-rich  $\gamma\text{-TiAl}$  phase. The results presented in this work allowed for characterization of phase transformations occurring in the as-deposited state that led to this final Laves /  $\gamma$  microstructure. Although the C14-type binary  $\text{TiCr}_2$  Laves phase is suggested to be present at relatively elevated temperatures ( $>1271^\circ\text{C}$ ) it is known to be stabilized at lower temperatures by Al [28,35].

Therefore, its presence can be expected since the as-deposited coating contained around 57 at. % of Al. Moreover, it has been shown that the partially amorphous microstructure of the as-deposited coating begins to transform already upon heating up to  $850^\circ\text{C}$ , and starts with the formation of the  $\text{AlCr}_2$  phase. Since the HT-XRD results did not reveal the disappearance of other phases, it is suggested that this phase most likely crystallizes from amorphous regions at around  $700^\circ\text{C}$ . The Al solubility in the C14 phase is known to decrease with increasing temperature [28], thus after around 4 h at  $850^\circ\text{C}$  it is rejected from the Laves phase and gives rise to the formation of the  $\text{TiAl}$  phase, that is most likely facilitated by further elemental diffusion from amorphous regions. At this stage the strong texture of the coating is most likely lost and it remains polycrystalline during further oxidation. This transformation from the textured and columnar microstructure to the somewhat equiaxed one may explain the formation of the voids observed after the oxidation test. The formation of the  $\gamma\text{-TiAl}$  and  $\text{AlCr}_2$  phases as well as the disappearance of the amorphous component may lead to volumetric changes facilitating the formation of voids. Another explanation for the void formation may be related to the Kirkendall effect, commonly observed in diffusion coatings on Ni-base superalloys [23,36]. The results presented in this work indicate that Al diffuses outwards to the growing oxide scale, and inwards to the substrate alloy. Additionally, Cr was found to diffuse inwards leading to formation of the diffusion zone, shown in Fig. 8b. It is suggested that these inward fluxes of Cr and Al are not balanced by the outward diffusion of other elements from the substrate resulting in a vacancy supersaturation and void formation. Moreover, after the 288 h at  $850^\circ\text{C}$  it has been shown using TEM that nanometric  $\alpha_2\text{-Ti}_3\text{Al}$  platelets start to form in equilibrium with the  $\gamma\text{-TiAl}$  phase. This  $\gamma$  to  $\alpha_2$  transformation has been suggested to originate from the depletion of Al due to high temperature oxidation and oxide scale growth [17]. However, longer exposures would be necessary for it to affect the oxidation behavior.

#### 4.3. High temperature oxidation behavior - role of Cr, Si and Y

The as-deposited coating was characterized by a uniform distribution of all the elements, i.e. Ti, Al, Cr, Y and Si. During the initial several hours at  $850^\circ\text{C}$  phase transformations took place that led to crystallization of major amounts of C14 Laves  $\text{Ti(Al,Cr)}_2$  and  $\gamma\text{-TiAl}$  phases. Moreover, minor nanometric precipitates of  $\text{Y}_2\text{O}_3$  and Si-rich C14  $\text{TiCr}_2$  were found.

It is well established that the reactive elements, such as Y, Hf and Zr significantly improve the high temperature oxidation resistance of Ni-base superalloy and coatings. Numerous publications have reviewed the potential mechanisms of their effect on the reduction of oxidation rate, counteracting the detrimental effect of sulfur or improving oxide scale adhesion [22,37,38]. In case of Ni-base superalloys it has been demonstrated that Y, Hf and Zr diffuse from the substrate to the scale-gas

interface along the grain boundaries of  $\alpha$ - $\text{Al}_2\text{O}_3$  scales in the oxygen potential gradient [39,40]. These elements are believed to affect the growth mechanism of  $\alpha$ - $\text{Al}_2\text{O}_3$  oxide scales by either “site blocking” [22] or reduction of Al ionization [41]. However, their effect and behavior on the oxidation mechanism of TiAl-base alloys has not been explored to the same extent as in the case of Ni-base superalloys. Several research works indicated the improvement of high temperature oxidation resistance of TiAl alloys by small additions of Y [18,42–45]. It has been found that the optimum amount of Y necessary to provide lowest mass gains during oxidation at 800–900 °C is around 0.3 at. % [18,44] since higher amounts lead to excessive formation of  $\text{Y}_2\text{O}_3$ , providing fast diffusion paths for oxygen. Moreover, the addition of Y leads to suppression of outer titania scale formation [19], although other research works indicated that excessive Y amounts may promote the formation of titania moulds and non-protective oxide scales [45]. The addition of Y to magnetron sputtered Al coatings was found to provide significant improvement in the hot corrosion and oxidation resistance of TiAl [46,47]. In the case of the studied system a very thin titania layer characterized by around 60 nm of thickness was found. All these works were in agreement that a proper addition of Y to TiAl promotes the growth of stable and protective  $\text{Al}_2\text{O}_3$  scale [18]. In this regard, the current study showed clearly that the behavior of Y in TiAl alloys is similar to that observed in case of Ni-base superalloys. In fact, it has been demonstrated for the first time that Y segregates to the  $\text{Al}_2\text{O}_3$  grain boundaries formed on TiAl, exactly as it is observed with alumina scales on Ni-base base superalloys [39,40,48,49]. Moreover, it is very likely that this is not a static but dynamic phenomenon, i.e. there is a continuous flux of yttrium diffusion from the coating to the oxide scale in the oxygen potential gradient (OPG) [50].

Research works that showed the positive effect of yttrium on the oxidation resistance of TiAl-based intermetallics indicated also that this element can be found in form of  $\text{Y}_2\text{O}_3$  at the boundaries of  $\gamma$ -TiAl phase. This was suggested to occur due to very high affinity of Y to oxygen and its solubility in  $\gamma$ -TiAl phase, both of which lead to the occurrence of oxygen scavenging effect [42,43]. Similar effect has been observed in the studied coating, where nanometric  $\text{Y}_2\text{O}_3$  precipitates were found within the  $\gamma$ -TiAl grains. Since the oxygen solubility in the  $\gamma$ -TiAl phase is less than approximately 1 at.% [8] it is likely that the excess Y is rejected and subsequently reacts with oxygen during high temperature oxidation.

The microstructure of the oxide scale formed on the studied coating is similar to that shown in other research works [13,17], where the formation of internal “oxide pockets” was observed. Since the Ti-Al-Cr coatings contain the  $\text{Ti}(\text{Al,Cr})_2$  Laves and  $\gamma$ -TiAl phases, where the former has a lower oxygen solubility and therefore higher oxidation resistance [8], it is suggested that these pockets form due to selective oxidation of the latter phase. It is further supported by the presence of unoxidized Laves phase visible between the outer very thin oxide scale (Fig. 11) and the internal  $\alpha$ - $\text{Al}_2\text{O}_3$  grains. The outer oxide scale, on the other hand, is believed to form as a result of Laves phase oxidation. It is strongly supported by the STEM results that revealed the presence of a very thin (around 90 nm) and continuous (Fig. 11) layer composed of equiaxed  $(\text{Al,Cr})_2\text{O}_3$ . This microstructural observation supports the idea that the role of Cr is the promotion of alumina formation, most likely by nucleation of chromia or Cr-doped alumina, during the initial stages of oxidation. Similar effect has been proposed by Fox-Rabinovich et al. [10], who detected, using AES and SIMS, the formation of Cr-rich oxides at the onset of oxidation. Underneath this equiaxed Cr-doped alumina observed in this study, a columnar layer was developed during the oxidation experiment. Both these layers are believed to be composed of the stable  $\alpha$  polymorph of alumina, as their equiaxed/columnar microstructure resembles very closely the oxide scales formed on Ni-base or FeCrAl alloys [40,51].

In addition to the role of Cr and Y, a direct role of Si on the growth of the oxide scale has not been observed in this study. Other research works indicated the positive effect of Si on the high temperature oxidation of

TiAl alloys and coatings applied on them [52–54]. It has also been suggested that combination of Hf, Y and Si leads to refined grain size and columnar structure of the oxide scale. However, it is not known to what extent silicon influences this phenomenon. One finding from this study is that Si segregates to the C14 Laves phase, which has been shown both in the micro (Fig. 7) as well as on the nano scale (Figs. 9 and 10). This may indicate a stabilizing effect of Si on its formation.

## 5. Summary

The paper presents the application of the CHC-PVD method for deposition of a protective Ti-Al-Cr-Y-Si coating on 48-2-2  $\gamma$ -TiAl alloy. In the as-deposited state the obtained coating was found to be characterized by a columnar microstructure that contained both amorphous and crystalline regions. During the initial stages of high temperature oxidation at 850 °C the crystallization of the coating occurred and involved the partial transformation of the textured Laves  $\text{TiCr}_2$  phase to  $\gamma$ -TiAl phase. During 288 h of oxidation at 850 °C the coating provided a significantly lower mass gain compared to the bare  $\gamma$ -TiAl alloy - around 0.35 mg/cm<sup>2</sup>. The high temperature oxidation resistance of the coating was owed to the formation of a very thin oxide scale composed of around 60 nm of titania, 90 nm of equiaxed  $(\text{Al,Cr})_2\text{O}_3$  and 70 nm of columnar  $\text{Al}_2\text{O}_3$ .

Yttrium has been found to segregate to the grain boundaries of the  $\alpha$ - $\text{Al}_2\text{O}_3$ , which is more commonly observed in case of Ni-base superalloys. Moreover, microstructural evidence has been presented that Cr segregates to the 90 nm thick layer of equiaxed  $(\text{Al,Cr})_2\text{O}_3$  layer, which supports the previous findings that it facilitates the formation of protective alumina scale.

## CRedit authorship contribution statement

**Radosław Swadźba:** Conceptualization, Methodology, Investigation, Resources, Writing - original draft, Writing - review & editing, Visualization, Supervision, Project administration, Funding acquisition.  
**Peter-Philipp Bauer:** Investigation, Methodology, Writing - original draft, Writing - review & editing, Visualization.

## Declaration of Competing Interest

The authors declare that they have no known competing financial interests or personal relationships that could have appeared to influence the work reported in this paper.

## Acknowledgements

This work was sponsored by the National Science Centre, Poland under contract UMO-2016/23/G/ST5/04128 and by Deutsche Forschungsgemeinschaft (DFG), Germany under contract Schu1372/6-1 within the Beethoven II programme - TiAlMET project.

## References

- [1] Y.W. Kim, S.L. Kim, *JOM* 70 (2018) 553–560.
- [2] B.P. Bewlay, S. Nag, A. Suzuki, M.J. Weimer, *TiAl Alloys in Commercial Aircraft Engines*, Taylor & Francis, 2016.
- [3] F. Dettewanger, E. Schumann, M. Ruhle, J. Rakowski, G.H. Meier, *Oxid. Met.* 50 (1998) 269–307.
- [4] S. Becker, A. Rahmel, M. Schorr, M. Schütze, *Oxid. Met.* 38 (1992) 425–464.
- [5] R. Swadźba, K. Marugi, Ł. Pyclik, *Corros. Sci.* 169 (2020) 108617.
- [6] M. Schütze, *JOM* 69 (2017) 2602–2609.
- [7] M.P. Brady, W.J. Brindley, J.L. Smialek, I.E. Locci, *JOM* 48 (1996) 46–50.
- [8] M.P. Brady, J.L. Smialek, J. Smith, D.L. Humphreys, *Acta Mater.* 45 (1997) 2357–2369.
- [9] M.P. Brady, J.L. Smialek, D.L. Humphrey, J. Smith, *Acta Mater.* 45 (1997) 2371–2382.
- [10] G.S. Fox-Rabinovich, G.C. Weatherly, D.S. Wilkinson, A.I. Kovalev, D.L. Wainstein, *Intermetallics* 12 (2004) 165–180.
- [11] K.L. Luthra, *Oxid. Met.* 36 (1991) 475–490.
- [12] N. Laska, R. Braun, *Mater. High Temp.* 32 (2015) 221–229.

- [13] N. Laska, R. Braun, S. Knittel, *Surf. Coatings Technol.* 349 (2018) 347–356.
- [14] R. Braun, K. Kelm, M. Fröhlich, C. Leyens, *Surf. Coatings Technol.* 222 (2013) 128–134.
- [15] R. Braun, M. Fröhlich, W. Braue, C. Leyens, *Surf. Coatings Technol.* 202 (2007) 676–680.
- [16] C. Leyens, J.W. Van Liere, M. Peters, W.A. Kaysser, *Surf. Coatings Technol.* 108–109 (1998) 30–35.
- [17] M. Fröhlich, R. Braun, C. Leyens, *Surf. Coatings Technol.* 201 (2006) 3911–3917.
- [18] Y. Wu, Y. Umakoshi, X.W. Li, T. Narita, *Oxid. Met.* 66 (2006) 321–348.
- [19] L.L. Zhao, G.Y. Li, L.Q. Zhang, J.P. Lin, X.P. Song, F. Ye, G.L. Chen, *Intermetallics* 18 (2010) 1586–1596.
- [20] G.S. Fox-Rabinovich, D.S. Wilkinson, S.C. Veldhuis, G.K. Dosbaeva, G. C. Weatherly, *Intermetallics* 14 (2006) 189–197.
- [21] N. Laska, R. Braun, *Oxid. Met.* 81 (2014) 83–93.
- [22] B.A. Pint, *Oxid. Met.* 45 (1996) 1–37.
- [23] R. Swadźba, J. Wiedermann, L. Swadźba, M. Hetmańczyk, B. Witala, U. Schulz, T. Jung, *Surf. Coatings Technol.* 260 (2014) 2–8.
- [24] R. Swadźba, *Appl. Surf. Sci.* 445 (2018) 133–144.
- [25] L. Kong, C. Wang, H. Zheng, X. Zhang, Y. Liu, *J. Phys. Chem. C* 119 (2015) 16623–16632.
- [26] R. Swadźba, N. Laska, P. Bauer, H. Krztoń, *Corros. Sci.* 177 (2020) 1–11.
- [27] R. Swadźba, *Unpubl. Data* (2020).
- [28] V. Raghavan, *J. Phase Equilibria Diffus.* 26 (2005) 349–356.
- [29] F. Huang, J.A. Barnard, M.L. Weaver, *Surf. Coatings Technol.* 155 (2002) 146–151.
- [30] Z. Tang, F. Wang, W. Wu, *Oxid. Met.* 48 (1997) 511–525.
- [31] J.A. Thornton, *Annu. Rev. Mater. Sci.* 7 (1977) 239–260.
- [32] B.A. Movchan, A.V. Demchishin, *Fiz. Met. i Met.* 28 (1969) 83–90.
- [33] I. Petrov, P.B. Barna, L. Hultman, J.E. Greene, *J. Vac. Sci. Technol. A Vacuum Surfaces, Film.* 21 (2003) S117–S128.
- [34] P.B. Barna, M. Adamik, *Thin Solid Films* 317 (1998) 27–33.
- [35] T.J. Jewett, M. Dahms, *Z. Met.* 87 (1997) 254–261.
- [36] P. Audigié, A. Rouaix-Vande Put, A. Malié, P. Bilhé, S. Hamadi, D. Monceau, *Surf. Coatings Technol.* 260 (2014) 9–16.
- [37] D.P. Whittle, J. Stringer, *Philos. Trans. R. Soc. A Math. Phys. Eng. Sci.* 295 (1980) 309–329.
- [38] D. Naumenko, B.A. Pint, W.J. Quadackers, *Oxid. Met.* 86 (2016) 1–43.
- [39] K.A. Unocic, Y. Chen, D. Shin, B.A. Pint, E.A. Marquis, *Micron* 109 (2018) 41–52.
- [40] R. Swadźba, L. Swadźba, J. Wiedermann, M. Hetmańczyk, B. Witala, *Oxid. Met.* 82 (2014) 195–208.
- [41] A.H. Heuer, T. Nakagawa, M.Z. Azar, D.B. Hovis, J.L. Smialek, B. Gleeson, N.D. M. Hine, H. Guhl, H.-S. Lee, P. Tangney, W.M.C. Foulkes, M.W. Finnis, *Acta Mater.* 61 (2013) 6670–6683.
- [42] Y. Wu, S.K. Hwang, S.W. Nam, N.J. Kim, *Scr. Mater.* 48 (2003) 1655–1660.
- [43] Y. Wu, S.K. Hwang, *Acta Mater.* 50 (2002) 1479–1493.
- [44] Y. Wu, K. Hagihara, Y. Umakoshi, *Intermetallics* 13 (2005) 879–884.
- [45] Y. Wu, K. Hagihara, Y. Umakoshi, *Intermetallics* 12 (2004) 519–532.
- [46] H. Lin, W. Liang, Y. Jia, Q. Miao, R. Hu, Z. Ding, L. Yu, *Appl. Surf. Sci.* 487 (2019) 868–875.
- [47] H. Lin, W. Liang, Q. Miao, S. Li, Z. Ding, S. Cui, J. Yi, Y. Qi, Z. Yang, H. Yu, *Appl. Surf. Sci.* 522 (2020), 146439.
- [48] B.A. Pint, A.J. Garratt-Reed, L.W. Hobbs, *Oxid. Met.* 56 (2001) 119–145.
- [49] K.A. Unocic, B.A. Pint, *Surf. Coatings Technol.* 205 (2010) 1178–1182.
- [50] B. Pint, A.J. Garratt-Reed, L.W. Hobbs, *J. Am. Ceram. Soc.* 14 (1998) 305–314.
- [51] B.A. Pint, *John Stringer Symp. High Temp. Corros. Mater. Park. ASM Int.* (2003) 1–10.
- [52] J.W. Fergus, *Mater. Sci. Eng. A* 338 (2002) 108–125.
- [53] R. Swadźba, L. Swadźba, B. Mendala, P.P. Bauer, N. Laska, U. Schulz, *Surf. Coatings Technol.* 403 (2020) 126361.
- [54] J. Wang, L. Kong, J. Wu, T. Li, T. Xiong, *Appl. Surf. Sci.* 356 (2015) 827–836.